Journal of Nuclear Medicine, published on October 23, 2020 as doi:10.2967/jnumed.120.250597

Performance evaluation of the uEXPLORER Total-body PET/CT scanner based on NEMA NU 2-2018 with additional tests to characterize long axial field-of-view PET scanners

Benjamin A. Spencer[1,2*], Eric Berg[1*], Jeffrey P. Schmall[3], Negar Omidvari[1], Edwin K. Leung[1], Yasser G. Abdelhafez[2], Songsong Tang[4], Zilin Deng[4], Yun Dong[4], Yang Lv[4], Jun Bao[4], Weiping Liu[4], Hongdi Li[3], Terry Jones[2], Ramsey D. Badawi[2,1] and Simon R. Cherry[1,2]

([*] authors contributed equally)

Affiliations: [1]Departments of Biomedical Engineering and [2]Radiology, University of California-Davis, Davis, CA, [3]United Imaging Healthcare, America, [4]United Imaging Healthcare, Shanghai, China.

Corresponding Author: Benjamin A. Spencer,

EXPLORER Molecular Imaging Center

UC Davis Health

3195 Folsom Blvd., Suite 120

Sacramento, CA 95816

Tel: 916-731-9005

Email: benspencer@ucdavis.edu

Word count: 8,012

Financial Support: Funding for this work was provided by NIH grant R01 CA206187, which is supported by NCI, NIBIB and the Office of the Director, and by R01 CA249422.

Disclosure: UC Davis has a research agreement and a sales-based revenue sharing agreement with United Imaging Healthcare. No other potential conflicts of interest relevant to this article exist including employment, royalties, stock options, or patents.

Running title: Performance evaluation of the uEXPLORER

ABSTRACT

The world's first total-body PET scanner with an axial field-of-view (AFOV) of 194 cm is now in clinical and research use at our institution. The uEXPLORER PET/CT scanner, developed through a collaboration between the University of California, Davis (UC Davis) and United Imaging Healthcare (UIH), is the first commercially available total-body PET scanner. Here we present a detailed physical characterization of the uEXPLORER PET scanner based on NEMA NU-2-2018 along with a new set of measurements devised to appropriately characterize the total-body AFOV.

Methods: Sensitivity, count-rate performance, time-of-flight resolution, spatial resolution, and image quality were evaluated following the NEMA NU-2-2018 protocol. Additional measurements of sensitivity and count-rate capabilities more representative of total-body imaging were performed using extended geometry phantoms based on the world average human height (~165 cm). Lastly, image quality throughout the long AFOV was assessed with the NEMA image quality (IQ) phantom imaged at five axial positions and over a range of expected total-body PET imaging conditions (low dose, delayed imaging, short scan duration).

Results: Our performance evaluation of the uEXPLORER PET system demonstrates that the scanner provides a very high sensitivity of 174 kcps/MBq, count-rate performance with a peak noise equivalent count-rate (NECR) of approximately 2 Mcps for total-body imaging, coupled with good spatial resolution capabilities for human imaging (≤ 3.0 mm FWHM near the center of the AFOV). Excellent image quality, contrast recovery, and low noise properties were illustrated across the AFOV in both NEMA IQ phantom evaluations and human imaging examples.

Conclusions: In addition to standard NEMA NU-2-2018 characterization, a new set of measurements based on extending NEMA NU-2-2018 phantoms and experiments were devised to

characterize the physical performance of the first total-body PET system. Rationale for these extended measurements was evident from differences in sensitivity, count-rate – activity relationships, and NECR limits imposed by differences in deadtime and randoms fraction between the NEMA NU-2 70 cm phantoms and the more representative total-body imaging phantoms. Overall, the total-body uEXPLORER PET system provides ultra-high sensitivity that supports excellent spatial resolution and image quality throughout the FOV in both phantom and human imaging.

Key Words: PET; EXPLORER; total-body imaging; performance evaluation

INTRODUCTION

The University of California, Davis (UC Davis) and United Imaging Healthcare (UIH) have collaborated to develop the world's first total-body PET scanner. The uEXPLORER PET/CT scanner has an axial field-of-view (AFOV) of 194.0 cm allowing PET data collection from the entire human body simultaneously and greatly increasing PET scanner sensitivity.

Previous simulation studies have demonstrated the sensitivity gain that is expected to be provided with long AFOV scanners (*1-7*). Work from Poon *et al.* (*1,2*) suggests that a 2-meter long LSO-based PET scanner would provide a sensitivity gain of approximately 40-fold for whole-body imaging compared to a conventional PET scanner with an axial length of 21.8 cm.

The sensitivity gain offered by long AFOV PET scanners opens up new possibilities for numerous research and clinical applications including: PET imaging with a much lower injected dose, late time point imaging, very fast imaging, and simultaneous total-body dynamic PET image acquisition (*8,9*). These potential breakthrough applications in clinical and research imaging (*8,9*) led to the creation of the EXPLORER consortium in 2011 (*10*). Through this consortium, UC Davis and UIH collaborated to design, develop, and manufacture the world's first total-body PET scanner (uEXPLORER). Fabrication of the PET/CT scanner was completed in May 2018 and uEXPLORER was granted 510(k) clearance from the US FDA in December 2018. The uEXPLORER scanner was installed at the EXPLORER Molecular Imaging Center (UC Davis Health) in May 2019 (Figure 1) with the first human imaging studies following in June 2019 and routine clinical use starting in August 2019. The EXPLORER consortium also supported development of the PennPET EXPLORER, a prototype PET scanner with a 64 cm AFOV (*11,12*), based on digital silicon photomultipliers (SiPM) detectors with direct crystal coupling. The

performance evaluation of the PennPET EXPLORER reported state-of-the-art time-of-flight (TOF) resolution of 256 ps and high sensitivity (55 cps/kBq).

Previous studies have identified the advantages of longer AFOV PET scanners (*13,14*) although all other state-of-the-art commercial scanners still range from 15 – 30 cm in AFOV (*15-22*). Watanabe *et al*. developed a 68.5 cm-long AFOV prototype PET scanner as early as 2004 (*13*) with a sensitivity of 9.72 cps/kBq. Conti *et al.* also developed a 53 cm-long AFOV PET scanner (*14*), which achieved a sensitivity of 19.87 cps/kBq; however, these scanners were never put into commercial production. Recently, a long axial FOV PET/CT prototype was developed by Siemens with axial length of approximately 1-meter (*23*). Additionally, cost-effective total-body imaging with plastic scintillators (J-PET) is in research development with several constructed prototypes (*24*).

In preliminary human studies with the uEXPLORER, Badawi *et al.* demonstrated the capability of performing low dose imaging (25 MBq ^{18}F-FDG), late time point imaging (10 hours post-^{18}F-FDG injection), fast imaging (<20 second static images), and simultaneous total-body dynamic imaging (*25*). Additionally, Zhang *et al.* reported total-body PET imaging with dynamic frames of just 100 ms to visualize cardiac motion (*26*). Here, we report a detailed physical characterization of the uEXPLORER PET/CT system using standard and newly designed phantom measurements to quantify important imaging metrics, including spatial resolution, count-rate performance, and quantitative image quality.

Characterization of PET scanners has commonly followed the National Electrical Manufacturers Association (NEMA) NU-2 standards (*27*), which defines a set of experiments and analyses using standardized imaging phantoms and permits valid comparisons to be made between different PET systems. While the NEMA NU-2-2018 measurements are performed in this

characterization of the uEXPLORER scanner, these standards are defined only for PET scanners with AFOV ≤65 cm and are not well suited for long AFOV scanners, especially the 194 cm long uEXPLORER, which is considerably longer than the 70 cm phantoms prescribed in the NEMA NU-2 tests. Therefore, a major component of this study was to devise a set of additional informative phantom measurements using extended phantom geometries and experiments that represent total-body imaging and provide a representative performance evaluation of uEXPLORER for total-body PET imaging. For these extended phantoms, lengths close to the world average human height (165 cm (*28*)) were chosen. By making use of standard phantom components already in practice for the NEMA NU-2 tests that are commonly followed in the literature, the extended phantom measurements are intended to serve as a reasonable and applicable starting point in the standardized characterization of long AFOV PET systems. Lastly, we note that all system and image evaluations were performed using in-house software developed at UC Davis.

MATERIALS AND METHODS

System Parameters

Physical Parameters of the Scanner. The uEXPLORER system is composed of 8 PET units along the axial direction; each unit is 24.02 cm in axial length, 78.6 cm in diameter (detector face-to-face), and with a 0.26 cm gap between units, forming the system's total axial length of 194.0 cm. There are 24 detector modules in each PET unit, and each module contains 70 block-detectors arranged in a 5 × 14 matrix (transaxial × axial). The detector blocks are composed of a 7 × 6 array of pixelated LYSO crystals, each 2.76 × 2.76 × 18.1 mm^3, that are read out using four 6 × 6 mm^2 SiPMs (SensL J-series). An integrated light guide design is used to encode the crystal position

among the four SiPM signals, achieving an Anger multiplexing of 10.5:1. Detectors along the transaxial direction of the module share energy information so that Compton-scattered photons from edge crystals can be recovered; axial blocks are not in communication for Compton scatter recovery. The uEXPLORER system is composed of 13,440 detector blocks with a total of 564,480 LYSO crystals and 53,760 SiPM channels. The PET system is integrated with a 160-slice CT scanner, capable of helical acquisition (maximum rotation speed of 0.5 sec) with minimum slice thickness of 0.5 mm. A patient bed designed to accommodate total-body PET imaging provides precise alignment (< 2 mm fusion accuracy) between PET and CT and with matched deflection.

Data Acquisition and Image Reconstruction. Each PET unit can form coincidence events with unit differences up to ±4, for a maximum acceptance angle of 57.0°, and is fixed by the manufacturer and used for all tests in this study except the NEMA NU-2-2018 spatial resolution test. The total number of lines-of-response (LORs) collected are 92 x 10^9. A variable coincidence timing window is used for both prompt and delayed coincidence channels to accommodate the large range of possible LOR lengths with the large acceptance angle: for unit differences of 0 the coincidence timing window is 4.5 ns, while for the maximum unit difference of four, a coincidence timing window of 6.9 ns is used. The time-of-flight (TOF) measurement is discretized in 39.06 ps bins. The scanner uses an energy window of 430 - 645 keV.

An 8-node computational cluster (vendor-provided) is used for data acquisition and image reconstruction. Raw coincidence data from each PET unit are transferred and stored locally on the computational cluster using a 10 Gbps network, allowing for event rates up to 149 Mcps per PET unit. Before reconstruction, these data are merged to form a single time-ordered list-mode file. The cluster is used for the parallel list-mode TOF-ordered subset, expectation maximization (OSEM)

reconstruction framework with graphics processing unit acceleration. Image reconstruction with point-spread function (PSF) modeling in projection space is provided.

Our typical clinical image reconstruction protocol is performed with four TOF-OSEM iterations, 20 subsets, 2.344 mm isotropic voxel size, with and without PSF modeling. Unless otherwise stated, all images were reconstructed with our clinical image reconstruction protocol with PSF modeling. While often unavoidable in conventional PET, no image smoothing or filtering was applied to the reconstructed images in this study to best demonstrate the image quality and noise levels.

Data Corrections and Calibrations. A non-paralyzable response model was used for deadtime correction at the level of each detector block; this level of discretization was determined from previous studies (*29*) and accounts for the large count-rate differences encountered across the AFOV in a total-body scanner. Correction factors were obtained from a measurement using a uniform cylindrical phantom (15 cm in diameter, 210 cm in length) with an initial activity of ~1,480 MBq (~40 mCi). The singles- count-rates of each block are recorded in the list-mode file and are used to estimate the deadtime loss for each coincident event, along with plane efficiency factors to account for oblique LORs (*29*). Normalization factors for detector efficiency and plane efficiency are also calculated using the data from the uniform cylindrical phantom (*30*). Scatter correction is performed using a Monte Carlo simulation-based method (*31*). A primary motivation of this method is to model multiple scatter events, which are more abundant in oblique LORs (*32*). Random coincidences are estimated using a delayed coincidence window implemented into the coincidence electronics hardware. The co-registered CT image is used for attenuation correction.

Sensitivity

System sensitivity was measured with two phantoms: a 70 cm line source (NEMA NU-2-2018) and a 170 cm line source, both filled with a low activity of ^{18}F (approximately 4 MBq). The 70 cm line source measurement followed the NEMA NU-2-2018 protocol that uses a set of five concentric aluminum sleeves to estimate attenuation-free sensitivity, while the 170 cm line source measurement was obtained without aluminum sleeves with the assumption of negligible 511 keV photon attenuation from the line source and sufficient stopping power of the emitted positrons in the 2 mm tubing wall thickness. The 170 cm filled tube line source was fastened to a taut guide line parallel to the axis of the scanner, attached on one end to the patient bed and on the opposite end to an external support positioned outside the scanner bore. Minimal (< 5 mm) deflection was observed along the line source length in reconstructed images. List-mode data from the system were binned into single-slice rebinned (SSRB) sinograms and used to estimate the total sensitivity and axial slice sensitivity for both phantom lengths. Similar to the NEMA NU-2-2018 analysis methodology for sensitivity, the 170 cm line source axial sensitivity profile was calculated by dividing the prompt minus delay count rate obtained from each SSRB sinogram slice by the total activity in the line source, and the total sensitivity was computed as the sum of all SSRB sinogram slices. The line source activity was normalized according to the actual extent of the line source filled with ^{18}F solution (169.7 cm) relative to the nominal 170 cm length.

Count Rate Performance

Count-rate performance of the uEXPLORER was assessed using a 70 cm-long NEMA NU-2-2018 scatter phantom and a 175 cm-long scatter phantom that was built using 10 segments from three NEMA NU-2-2018 scatter phantoms (Data Spectrum, Durham N.C., USA). Both phantoms

include a fillable line source that is threaded through the length of the phantom. Count-rates for trues, scatters, and random coincidences were extracted from prompt and delayed coincidence SSRB sinograms using the methods outlined in NEMA NU-2-2018 for both phantom lengths. Noise equivalent count-rate (NECR) was computed assuming a low variance randoms estimate, i.e. with a randoms multiplier of 1. The ideal trues rate was estimated using a linear fit of the measured trues at low activity where deadtime losses are assumed negligible, and the difference between the extrapolated ideal trues and measured trues was used to estimated deadtime losses at each measured activity. Only the SSRB sinogram slices within the central 65 cm of the AFOV were used for the 70 cm-long phantom as specified in NEMA NU-2-2018, while similarly the central 170 cm SSRB sinograms were used for the 175 cm-long phantom. Both line sources were filled with approximately 1100 MBq of ^{18}F at the start of the experiments.

Time-of-Flight Resolution

Time-of-flight (TOF) resolution was calculated according to the NEMA NU-2-2018 protocol that measures TOF resolution from the list-mode data generated in the 70 cm scatter phantom count-rate experiment. Only prompt coincidences traversing within +/- 20 mm from the line source are included, and the list-mode TOF values after correction for the position of the line source relative to the midpoint of the LOR are binned into a TOF histogram and used to compute FWHM coincidence timing resolution. Subtraction of scatter and random coincidences is performed as described in NEMA NU-2-2018 using the tails of the TOF histograms. The vendor provided timing offset corrections were applied during the list-mode processing step.

Time-of-flight resolution for individual LORs was also computed using a subset of the LORs that contain sufficiently large number of counts. To acquire enough counts, a 37 MBq ^{68}Ge line

source was used in place of the ^{18}F line source in the NEMA NU-2-2018 scatter phantom and list-mode data was acquired for ~12 hours. The same TOF processing was used as described for the NEMA NU-2-2018 TOF measurement, except exclusions were applied during processing to select events from individual LORs.

Spatial Resolution

NEMA NU-2-2018 spatial resolution was measured by imaging 0.5 mm inner-diameter ^{18}F (~300 kBq) capillary sources with <1 mm axial extent. To perform the analytic reconstruction as specified in the NEMA NU-2-2018 guidelines, the list-mode data were first Fourier re-binned (FORE) into 2D sinograms (*33*) and the sinograms were reconstructed in 1023×1023 image matrices (0.6 mm × 0.6 mm pixels) using 2D filtered backprojection (FBP) (0.6 mm sinogram and image slice thickness). To minimize the Fourier re-binning error in the axial direction when using a large acceptance angle (34), the acceptance angle was restricted to the width of one unit (24 cm) for this measurement. The spatial resolution full-width half-max (FWHM) was computed following NEMA NU-2-2018. The presented data are an average of two separate measurements.

In addition, reconstructed spatial resolution with the 3-D OSEM algorithm and using the standard acceptance angle (+/- 4 units, 57°) was assessed using an ^{18}F-FDG (approximately 20 MBq) filled Mini-Derenzo phantom (Data Spectrum, Durham N.C., USA). The diameter and edge-to-edge spacing of the activity-filled hollow channels are 1.2 mm, 1.6 mm, 2.4 mm, 3.2 mm, 4.0 mm, and 4.8 mm. The phantom was imaged in two orientations (activity-filled rods in the transaxial plane and sagittal plane) and at two axial positions (axial center and center of the last PET unit i.e. 1/16th AFOV) to assess the effect of acceptance angle on reconstructed spatial resolution on both transaxial and axial resolution. Images were reconstructed with our high-

resolution brain reconstruction parameters (1.172 mm isotropic voxels, 10 iterations) and without PSF to unambiguously demonstrate changes in spatial resolution.

Image Quality and Accuracy of Corrections

The NEMA image quality (IQ) phantom was filled and imaged according to NEMA NU-2-2018. All spheres were filled with an ^{18}F-FDG solution at a sphere-to-background concentration ratio of 3.7:1, and with a background activity concentration of 5.1 kBq/mL. The IQ phantom was positioned with the spheres at the axial center of the PET FOV. A single bed position was used with a scan duration of 30-min.

Images were reconstructed using the clinical image reconstruction protocol (2.344-mm isotropic voxels, 4 iterations, 20 subsets), both with and without PSF modelling, in addition to our high-resolution brain reconstruction protocol (1.172-mm isotropic voxels, 10 iterations, 20 subsets) with PSF modelling. The contrast recovery coefficient (CRC), background variability, and relative count error in the cold lung region (ΔC_{lung}) were calculated using a semi-automated tool developed to define ROI boundaries and extract ROI statistics. In short, phantom center and sphere center coordinates were identified by parabolic fitting on regional image projections and 2D circular region-of-interest (ROI) analysis was performed, taking the partial pixels into account.

The NEMA IQ phantom and methodology was also used to assess image quality with reduced scan durations or reduced ^{18}F activity. The impact of scan duration on image quality was measured by reconstructing the shorter time frames from the original 30-min duration list-mode file to simulate shorter scan durations, as short as 30 s. The effect of the activity level on image quality was evaluated by scanning the NEMA IQ phantom at 18 time points, up to 12 hours delayed. The phantom was not moved between scans.

To evaluate the image quality throughout the AFOV the NEMA IQ and scatter phantom were scanned at axial positions of ± 39 cm and ± 63 cm from the center of the AFOV; axial location was defined by the center of the IQ spheres. These positions were chosen based on the axial sensitivity profile that correspond to roughly 95% and 70% of the peak sensitivity. The scan durations ranged from 7.6-min to 13.0-min from the first to last acquisition to account for ^{18}F radioactivity decay. This phantom measurement had a sphere-to-background concentration ratio of 5.2:1 and a background activity concentration of 4.5 kBq/mL at the start of imaging.

Lastly, given that the CRC may be dependent on the sphere-to-background ratio, in addition to the previously described two sets of scans with sphere-to-background concentration ratios of 3.7:1 and 5.2:1, an additional NEMA IQ scan was performed at the center of the AFOV using a sphere-to-background concentration ratio of 9.0:1. The specifications of all NEMA IQ scans used for this comparison are summarized in supplemental Table 1.

Human Imaging

Two studies from routine clinical care are presented to exemplify the uEXPLORER physical characterization results defined by phantom studies. The study data was collected through an institutional review board approved retrospective study, and a prospective study in which the subject signed a written informed consent. (1) A prostate cancer patient imaged for 10-min at 4-min after injection of 320 MBq (8.6 mCi) of ^{18}F-Fluciclovine was used to demonstrate the spatial resolution characteristics in human imaging. (2) A lung cancer patient scanned for 20-min following a 90-min uptake period of 188 MBq (5.09 mCi) of ^{18}F-FDG was used to illustrate the image quality and sensitivity of the scanner. Image reconstructions of shortened durations were also performed to depict count dependent image quality. For both studies the fractional deadtime

was estimated from the count-rate experiment using the 175 cm scatter phantom at the equivalent activity concentration.

RESULTS

Sensitivity

The NEMA NU-2-2018 sensitivity of the uEXPLORER PET/CT with the 70 cm-long line source filled with ^{18}F was 174 kcps/MBq at the center of the FOV and 177 kcps/MBq at 10 cm radial offset. With the 170 cm-long line source, the total sensitivity was 147 kcps/MBq at the center, and 151 kcps/MBq at 10 cm radial offset. Axial sensitivity profiles (Figure 2) show a peak sensitivity plateau between ±48.5 cm from the center due to the maximum acceptance angle of ±4 ring units, with minor peaks and valleys within the plateau caused by the unit-difference-based coincidence selection that leads to peak sensitivity at the midpoints of the four central PET units. This contrasts with conventional PET scanners that use a maximum acceptance angle equal to that of the full axial extent of the system and therefore demonstrate triangular axial sensitivity profiles (*15-22*). The peak sensitivity estimated from the 170 cm line source axial sensitivity profile is approximately 18.6% (calculated by dividing the peak SSRB slice sensitivity (158 cps/MBq) by the fraction of activity contained in each slice (1 MBq / 1700 mm = 0.8 kBq / 1.44 mm). This is in close agreement with the NEMA NU-2-2018 sensitivity (174 kcps/MBq = 17.4%), and which is expected given the plateau shape of the NEMA NU-2-2018 sensitivity profile (Figure 2 A).

Count Rate Performance

Peak NECR with the 70 cm NEMA NU-2-2018 scatter phantom was 1,524 kcps at 17.3 kBq/mL activity concentration, with a corresponding average scatter fraction of 36.3%, Figure 3 C. With

the 175 cm-long scatter phantom, peak NECR increased to 1,855 kcps at 9.6 kBq/mL, with a corresponding average scatter fraction of 37.4%, Figure 3 D. At the peak NECR the estimated deadtime losses in the trues rate were 34% with both the 70 cm and 175 cm phantoms, shown in supplemental Figure 1. Peak NECR with the 175 cm phantom is in good agreement with simulations of a 2-meter long PET scanner (validated against the mCT scanner), and demonstrated a 25 – 31 fold increase in NECR vs. conventional PET systems (*1,2*).

Time-of-Flight Resolution

Time-of-flight (TOF) resolution measured with NEMA NU-2-2018 is shown vs activity concentration in Figure 4. Good TOF resolution stability is achieved, with <5% degradation from the lowest activity concentration up to the peak NECR activity concentration (17.3 kBq/mL). This minor decrease in TOF performance at higher activities may be related to pulse pile-up causing crystal misidentification, or other count-rate dependent factors in the front-end electronics (e.g. baseline noise). There were no discernable differences in TOF resolution between the NEMA NU-2-2018 70 cm long scatter phantom and the 175 cm scatter phantom as described. TOF resolution for individual LORs using the long duration ^{68}Ge scan (equivalent activity concentration of ~2 kBq/mL) was 412 +/- 35 ps. The average number of counts per LOR used to compute TOF resolution was ~2000.

Spatial Resolution

Spatial resolution measured according to NEMA NU-2-2018 with an ^{18}F point source and FORE-FBP reconstruction is summarized in Table 1. Reconstructed image slices of the Mini-Derenzo phantom are provided in Figure 5. In the transaxial orientation (i.e. radial and tangential

resolution components), there is negligible difference in spatial resolution between the axial center with maximum acceptance angle of 57.0 degrees and at the center of the last PET unit (1/16th AFOV) with a maximum acceptance angle of 17.0 degrees. The 2.4 mm rods are clearly resolved at both positions. In the sagittal orientation, the 2.4 mm rods are mostly resolved when scanned with one PET unit (1/16th AFOV), while the minimum rod resolvability is 3.2 mm at the axial center. This is in agreement with previous findings which demonstrated an approximately 0.5 mm degradation in axial spatial resolution with a similar acceptance angle comparison *(35)*.

Image Quality and Accuracy of Corrections

Contrast recovery and background variability results with the NEMA IQ phantom at the axial center of the FOV are shown in Figure 6. The choice of reconstruction parameters has a large impact on CRC, particularly for the smallest sphere (10 mm); using our clinical image reconstruction protocol with no PSF modelling the CRC is 49.8%, whereas with our high-resolution brain reconstruction parameters (1.17-mm voxels, 10 iterations) with PSF modelling it increases to 69.2%. The background variability is very low in all reconstruction modes and ROI sizes, ranging from 1.2% to 4.3%. The relative count error in the lung insert was 1.36% and 2.88% using the clinical image reconstruction protocol with and without PSF modelling, respectively, while it was 0.00% with the high-resolution brain reconstruction protocol.

Contrast recovery and background variability as a function of scan time and activity are shown in Figure 7. Contrast recovery is stable when reducing the scan duration or activity down to 30% of the standard values for all sphere sizes. Furthermore, the contrast recovery of the four larger spheres is not affected when reducing the scan time or activity down to 10%. Similarly, background variability stays below 7%, even for the 10 mm sphere size, when scan duration or

activity is decreased down to 10% of the original value. Example images of the central slice of the 30-min scan of the IQ phantom at 0, 3, 6, 9, and 12 hour delayed time points (Figure 7 E) gives a qualitative assessment of the image quality at different activity levels. Additional images with reduced scan times and activities are shown in supplemental Figure 2.

The evaluation of the uEXPLORER image quality throughout the AFOV is depicted in Table 2, which provides the CRC and background variability from five scans at five axial positions for two representative spheres (37 mm and 22 mm). The images of the five scans are shown in supplemental Figure 3. The results show that CRC is not significantly affected throughout the AFOV, whereas there is a small increase in background variability at the edges of the FOV where the scanner has lower sensitivity (70% compared to peak sensitivity at the center).

Finally, effect of sphere-to-background ratio on contrast recovery of all spheres is shown in supplemental Figure 4, in which CRC of the smallest sphere is improved to 93.9% with sphere-to-background ratio of 9.0:1.

Human Imaging

Human imaging results that illustrate the uEXPLORER scanner's spatial resolution, sensitivity, and overall image quality are provided in Figure 8. The acquisition parameters of these studies are summarized in Table 3, along with the singles, prompts, and randoms count-rates, and estimated deadtime fraction. Estimated deadtime for human studies was calculated using the deadtime fractions obtained with the 175 cm phantom experiment at the corresponding effective activity concentrations for each human PET exam (4.1 kBq/mL for the ^{18}F-fluciclovine subject and 1.4 kBq/mL for the ^{18}F-FDG subject).

The transaxial images shown in Figure 8 A demonstrate the uEXPLORER's excellent spatial resolution which enables clear tracer localization within a pulmonary nodule measured to be 2.5 mm in diameter on the CT.

The uEXPLORER's high sensitivity and image quality attributes can be displayed using reconstructions of shortened scan durations extracted from a representative 20-min ^{18}F-FDG PET scan in a lung cancer patient. This clinical oncology total-body PET protocol is achieved with half the standard injected activity (~185 MBq) and acquired 30-min later (90-min) compared to conventional whole-body PET at our institution, yet a 5-min acquisition still demonstrates excellent image quality. Although image noise noticeably increases with shorter acquisition times, all lesions, including a small (~1 cm) FDG-avid adrenal lesion, can be visualized in the 2.5-min acquisition.

In supplemental Figure 5, the effect of scan duration on coefficient of variation (CV) is shown for a homogeneous 37 mm dimeter spherical ROI placed in the patient liver and similarly in the background of the NEMA IQ phantom acquired at a similar activity concentration to that of the patient liver and with matched reconstruction parameters. We observe that the trend in CV vs scan duration of this human scan closely mirrors the trends of the CV measured in NEMA IQ phantom. The approximately 25% positive bias in CV in the liver compared to the phantom may be a result of patient motion (respiration), anatomical inhomogeneities, or differences in the accuracy of the data corrections (e.g. scatter, attenuation).

DISCUSSION

The dominant physical performance attribute of the uEXPLORER total-body PET system is its high sensitivity, which cannot be fully reflected with the NEMA NU-2-2018 standard. Therefore,

an alternative measurement with an approximately average human sized (*27*) 170-cm-long line source was required. If we extrapolate the published 70 cm NEMA NU-2-2018 sensitivities for state-of-the-art PET systems with conventional < 25 cm AFOV (*15*-*22*) to what would be obtained with the total-body 170-cm-long line source (i.e. multiply the published NEMA NU-2 values by 70 cm / 170 cm, which is a valid mathematical representation of the reduced activity per unit length in the 170 cm long line source measurement for scanners with AFOV of <70 cm), the 147 kcps/MBq total-body sensitivity of the uEXPLORER represents a 15 – 68 fold gain compared to current state-of-the-art conventional systems as predicted by the prior simulation work (*1,2*). While a wider acceptance angle than the fixed ±4 maximum unit difference would provide higher line source sensitivity, in practice for human imaging the optimal acceptance angle depends on several effects including the patient size and activity distribution and overall concentration and is a subject of future investigations. The high sensitivity provided by the 194 cm AFOV is further evident in the excellent image quality obtained with low activity imaging, short duration acquisitions, or considerably delayed scans (see Figures 7 & 8).

The total sensitivity is higher for the 70 cm line source compared to 170 cm as expected from the reduced geometric efficiency towards the ends of the scanner, however, the peak NECR with the 175 cm long scatter phantom is higher than with the 70 cm scatter phantom. This can be explained by differences in attenuation and deadtime losses that depend on the phantom length. First, by examining the slope of the ideal trues count rate vs total activity for both the 70 cm and 175 cm scatter phantoms (Supplemental Figure 1) yields very similar values for both phantom lengths. Although the sensitivity results suggest higher trues sensitivity for shorter line source phantoms, the impact of attenuation is greater in the 70 cm phantom at the center of the AFOV compared to the extended 175 cm phantom. This is due to the larger relative abundance of oblique

LORs with the 70 cm phantom at the axial center vs. the 175 cm phantom that extends close to the ends of the scanner where the acceptance angle is reduced.

Secondly, distributing a given amount of activity over a wider extent of the FOV with the longer phantom leads to lower average singles rates for the LORs that intersect the phantom compared to the axially concentrated activity distribution in the 70 cm scatter phantom. This results in reduced deadtime fraction with the 175 cm phantom vs the 70 cm phantom at matched levels of total activity. While the trues to deadtime loss ratio at the respective peak NECR activities was 34% for both phantom lengths, the longer phantom reaches peak NECR at a higher absolute activity, and therefore provides a higher absolute trues rate and NECR.

The remaining factor that impacts the NECR at high activities are the randoms. The use of a wide acceptance angle in the 194 cm long scanner necessitates the use of a relatively wide coincidence timing window for oblique LORs. So, while the absolute deadtime losses at each activity are lower with the 175 cm phantom, which therefore provides better trues linearity compared to the 70 cm phantom shown in Figure 3 and Supplemental Figure 1, this is eventually overwhelmed by the large increase in randoms at high activities and becomes the limiting factor for peak NECR. The small activity dependent increase in SF observed in both scatter phantom measurements may be a result of pulse pile-up that causes crystal misidentification in the flood maps, a common effect in PET systems that employ light sharing block detectors. However, a detailed investigation of the relationships between count-rates, NECR, and image quality metrics is needed in future work.

In supplemental Figure 1, the count-rates for both phantoms are plotted relative to absolute activity rather than activity concentration, and the described effects can be clearly seen: while the slope of the ideal trues count rates are nearly identical for both the 70 cm and 175 cm scatter

phantoms, indicating equivalent geometric trues sensitivity for both phantoms, the deadtime losses and deadtime fraction are universally lower in the 175 cm long scatter phantom vs the 70 cm long scatter phantom, and results in higher peak NECR with the longer phantom compared to the NEMA NU-2-2018 measurement. Measuring the NECR of a total-body PET scanner using a 70 cm phantom does not translate to a very useful metric for clinical total-body PET human imaging; however, the peak NECR for a human sized 175 cm phantom should directly translate to an estimate for the peak NECR during total-body human imaging with clinically appropriate activity levels. This observation further demonstrates the necessity for a new set of measurements to characterize total-body PET scanners.

The measured NECR characteristics have several implications for clinical use. First, the high peak NECR for both the 70 cm NEMA NU-2-2018 and extended 175 cm phantom measurements supports the use total-body PET for improving image quality (reduced statistical noise), the use of short frames (e.g. <= 1 second) for dynamic imaging, and reducing scan duration (< 1 minute). Although the NECR reaches its peak at an activity concentration above the concentrations encountered in all uEXPLORER studies to-date, some applications that involve highly concentrated and large total activities (e.g. ^{82}Rb, ^{15}O-H_2O) may be dose-limited, however a detailed investigation is needed in this regard.

The extended phantom measurements presented here are suitable for adoption in the characterization of other long axial FOV PET systems. While a 70 cm long phantom may well approximate the count rates encountered in conventional PET exams where a large fraction of the imaging subject and activity is outside the scanner FOV at any one time, extended axial FOV and single bed position imaging necessitates the use of phantoms with lengths that better represent the extent of the activity biodistribution in clinical PET studies. Therefore, we expect that our

presented phantom measurements with 170 – 175 cm phantoms that were modeled from the NEMA NU 2 standard will serve as a reasonable starting point for future long axial FOV scanner characterizations.

PET data correction methods currently used in uEXPLORER have been extended from conventional approaches. However, quantification in such a large system with the inclusion of highly oblique LORs poses many new challenges to the models and assumptions encountered in conventional PET data corrections. With the emphasis of this study being on physics characterization of the first total-body PET scanner, a complementary investigation of quantitation in total-body PET is soon forthcoming.

The discrepancy between the global TOF resolution (505 ps) and the average TOF resolution calculated from individual LOR TOF histograms (412 ps) likely indicates an incomplete TOF calibration. With >500,000 crystals forming almost 100 billion LORs, accurately calibrating the TOF offsets in the uEXPLORER is challenging using the existing methods that were developed for much shorter PET systems. Work in this area is ongoing.

The use of LYSO crystals with small cross-section provides spatial resolution of ~3 mm FWHM (see table 1), the smallest NEMA NU-2 resolution for any whole-body PET/CT system to date. Combined with its high sensitivity, the uEXPLORER is able to produce reconstructed images with small voxel sizes (e.g. 1.17 mm isotropic voxels) while maintaining lower background variability compared to conventional PET systems that universally use larger voxel sizes and post reconstruction smoothing (Figure 6). The increase in contrast recovery with small voxels coupled with low background variability is likely of high interest for clinical PET imaging, for example detecting and quantifying uptake in smaller lesions, although clinical validation is needed.

Comparing the image quality figures-of-merit obtained with the NEMA IQ phantom to conventional whole-body PET systems, the uEXPLORER offers high CRC, particularly for the small sphere sizes (10 mm and 13 mm), due to the fine spatial resolution provided by small detector pixel size. While no modifications were made to the spheres embedded in the NEMA IQ phantom for these measurements, recent developments in PET sensitivity and spatial resolution, including in this work most notably in the detection of sub-5 mm lung lesions with ^{18}F-fluciclovine, suggests precedence to revisit the standardized methods and phantom sphere sizes used to evaluate contrast recovery in clinical PET systems. Future evaluation studies with the total-body uEXPLORER system will include a detailed investigation of the detection limits in high sensitivity and high resolution total-body PET. As expected from the scanner's high sensitivity, background variability is approximately 1.8 to 3.0-fold lower than other current state-of-the-art conventional PET systems (*15-17,19-21,22*). Lastly, the similarity in image quality metrics obtained with reduced scan durations to those obtained with reduced activity concentration (delayed scan) suggests that the increased LYSO background radiation from the large volume of ^{176}Lu in the uEXPLORER compared to conventional PET systems has minimal impact on image quality for activity concentrations as low as approximately 0.1 kBq/mL.

A critical parameter in any PET system, but especially so in long-AFOV PET, is the uniformity of image quality throughout the AFOV. In long-AFOV PET however, this cannot be entirely characterized in a single scan with the available short-length image quality phantoms. To address this limitation, we imaged the NEMA IQ phantom at five different axial positions along the AFOV. Excellent uniformity in CRC and background variability was measured as the phantom moved from the center of the AFOV to ±63 cm offset from the center. With the two tested sphere sizes, the standard deviation of CRC and background variability at five axial positions was below 3%

and 0.3%, respectively. Importantly, consistent background variability measured within the central 125 cm span of the AFOV illustrates the result of the plateau in peak sensitivity within the central ~120 cm of the AFOV as shown in the total-body axial sensitivity profile (Figure 2 B), and which is provided uniquely by the 57.0 degree acceptance angle and the 194 cm total AFOV. Overall, the image quality evaluation suggest the uEXPLORER can provide excellent imaging capabilities for routine clinical studies, and in a variety of imaging regimes, spanning ultra-low dose, delayed imaging up to 12 hours with ^{18}F, and short dynamic frames.

CONCLUSION

The study describes the first performance evaluation of the 194 cm long uEXPLORER total-body PET/CT system using the standard NEMA NU-2-2018 measurements as well as newly devised measurements to fully characterize the long AFOV PET scanner that are not well served by the current NEMA NU-2 standards. The total-body system exhibits high sensitivity (174 kcps/MBq with NEMA NU-2-2018, 147 kcps/MBq with a 170 cm human-sized line source), and similarly high count-rate performance that follows from the high geometric sensitivity of the long AFOV system, with a peak NECR of 1,524 kcps with NEMA NU-2-2018 and 1,855 kcps for the extended 175 cm total-body imaging phantom. Count-rate results further indicate that NECR becomes limited by deadtime losses and a high randoms fraction beyond ~370 MBq . The small LYSO crystal size coupled with high sensitivity allows for spatial resolution of ~ 3.0 mm demonstrated in both phantom scans and clinical imaging. Together, these system attributes enable excellent image quality and low statistical noise in both phantom evaluations and clinical studies. This total-body PET system represents a step-change in performance which opens up a wide range of new opportunities in research to study total-body tracer kinetics in systemic and multi-organ

disease, and in clinical practice where protocols can be tailored to emphasize exceptional image quality, short scan durations, low radiation dose or delayed imaging as dictated by the clinical question at hand.

ACKNOWLEDGEMENTS

Funding for this work was provided by NIH grant R01 CA206187, which is supported by NCI, NIBIB and the Office of the Director, and by R01 CA249422. The authors would like to thank the EXPLORER Molecular Imaging Center clinical team especially Dr. Lorenzo Nardo, and Denise Caudle.

KEY POINTS

QUESTION: What is the performance of the first ever total-body PET scanner using standard NEMA NU-2-2018 tests, and how can these tests be extended to provide a more informative evaluation of PET scanners with an axial field of view that exceeds what was envisioned when the NEMA tests were devised?

PERTINENT FINDINGS: The EXPLORER total-body PET scanner exhibits the highest sensitivity and count-rate performance of any available PET/CT scanner, which coupled with its spatial resolution of ~ 3 mm produces a step change in image quality achievable with PET.

IMPLICATIONS FOR PATIENT CARE: This ultra-high sensitivity scanner is already being used in routine clinical service to decrease patient dose while at the same time dramatically improving image quality.

REFERENCES

1. Poon JK, Dahlbom ML, Moses WW, et al. Optimal whole-body PET scanner configurations for different volumes of LSO scintillator: a simulation study. *Phys Med Biol*. 2012;57:4077–4094.
2. Poon JK. *The Performance Limits of Long Axial Field of View PET Scanners* (thesis). Davis, CA: University of California, Davis; 2013.
3. Badawi RD, Lewellen TK, Harrison RL, Kohlmyer SG and Vannoy, SD. The effect of camera geometry on singles flux, scatter fraction and trues and randoms sensitivity for cylindrical 3D PET - a simulation study. *IEEE Trans Nucl Sci*. 47(3):1228-1232, 2000.
4. Surti S, Karp JS. Impact of detector design on imaging performance of a long axial field-of-view, whole-body PET scanner. *Phys Med Biol*. 2015;60:5343–5358.
5. Surti S, Werner ME, Karp JS. Study of PET scanner designs using clinical metrics to optimize the scanner axial FOV and crystal thickness. *Phys Med Biol*. 2013;58:3995–4012.
6. MacDonald LR, Harrison RL, Alessio AM, Hunter WCJ, Lewellen TK, Kinahan PE. Effective count rates for PET scanners with reduced and extended axial field of view. *Phys Med Biol*. 2011;56:3629–3643.
7. Couceiro M, Ferreira NC, Fonte P. Sensitivity assessment of wide axial field of view PET systems via Monte Carlo simulations of NEMA-like measurements. *Nucl Instrum Meth A*. 2007;580:485–488.
8. Cherry SR, Badawi RD, Karp JS, Moses WW, Price P, Jones T. Total-body imaging: transforming the role of positron emission tomography. *Sci Transl Med*. 2017;9:381.

9. Cherry SR, Jones T, Karp JS, Qi J, Moses WW, Badawi RD. Total-body PET: maximizing sensitivity to create new opportunities for clinical research and patient care. *J Nucl Med*. 2018;59:3–12.
10. Our team – EXPLORER total-body PET scanner – UC Davis. https://explorer.ucdavis.edu/our-team. Updated April 5, 2019. Accessed July 10, 2020.
11. Karp JS, Viswanath V, Geagan MJ, et al. PennPET Explorer: Design and preliminary performance of a whole-body imager. *J Nucl Med*. 2020;61:136–143.
12. Pantel AR, Viswanath V, Daube-Witherspoon M, et al. PennPET Explorer: human imaging on a whole-body imager. *J Nucl Med*. 2020;61:144–151.
13. Watanabe M, Shimizu K, Omura T, et al. A high-throughput whole-body PET scanner using flat panel PS-PMTs. *IEEE Trans Nucl Sci*. 2004;51:796–800.
14. Conti M, Bendriem B, Casey M, et al. Performance of a high sensitivity PET scanner based on LSO panel detectors. *IEEE Trans Nucl Sci*. 2006;53:1136–1142.
15. Hsu DFC, Ilan E, Peterson WT, Uribe J, Lubberink M, Levin CS. Studies of a next-generation silicon-photomultiplier-based time-of-flight PET/CT system. *J Nucl Med*. 2017;58:1511–1518.
16. van Sluis J, de Jong J, Schaar J, et al. Performance characteristics of the digital Biograph Vision PET/CT system. *J Nucl Med*. 2019;60:1031–1036.
17. Rausch I, Ruiz A, Valverde-Pascual I, Cal-Gonzalez J, Beyer T, Carrio I. Performance evaluation of the Vereos PET/CT system according to the NEMA NU2-2012 standard. *J Nucl Med*. 2019;60:561–567.

18. Jakoby BW, Bercier Y, Conti M, Casey ME, Bendriem B, and Townsend DW. Physical and clinical performance of the mCT time-of-flight PET/CT scanner. *Phys Med Biol*. 2011;56:2375–2389.
19. Bettinardi V, Presotto L, Rapisarda E, Picchio M, Gianolli L, Gilardi MC. Physical performance of the new hybrid PET/CT Discovery-690. *Med Phys*. 2011;38:5394–5411.
20. Kolthammer JA, Su KH, Grover A, Narayanan M, Jordan DW, Muzic RF. Performance evaluation of the Ingenuity TF PET/CT scanner with a focus on high count-rate conditions. *Phys Med Biol*. 2014;59:3843–3859.
21. Delso G, Fürst S, Jakoby B, et al. Performance measurements of the Siemens mMR integrated whole-body PET/MR scanner. *J Nucl Med*. 2011;52:1914–1922.
22. Grant AM, Deller TW, Khalighi MM, Maramraji SH, Delso G, Levin CS. NEMA NU 2-2012 performance studies for the SiPM-based ToF-PET component of the GE SIGNA PET/MR system. *Med Phys*. 2016;43:2334–2343.
23. Conti M, Bharkhada D, Cabello J, et al. Design considerations for an ultra-long axial FOV PET/CT scanner. *J Nucl Med*. 2020;61(suppl 1):314.
24. Niedzwiecki S, Bialas P, Curceanu C, et al. J-PET: a new technology for the whole-body PET imaging. *Acta Physica Polonica B*, 2017;48:1567.
25. Badawi RD, Shi H, Hu P, et al. First in human imaging studies with the EXPLORER total-body PET scanner. *J Nucl Med*. 2019;60:299–303.
26. Zhang X, Cherry SR, Zhaoheng X, Hongcheng S, Badawi RD, Qi J. Subsecond total-body imaging using ultrasensitive positron emission tomography. *Proc Natl Acad Sci*. 2020;117:2265-2267.

27. *NEMA standards publication NU 2-2018 – performance measurements of positron emission tomographs (PET)*. Rosslyn, VA: National Electrical Manufacturers Association; 2018.
28. NCD Risk Factor Collaboration (NCD-RisC) (2016). A century of trends in adult human height. *eLife* 2016;5:13410.
29. Tang S, Liu Y, Wang J, Zhao Y, Fan X, Dong Y. Dead time correction method for long axial field-of-view, whole-body PET scanner. *J Nucl Med*. 2019;60(suppl 1):458.
30. Tang S, Zhao Y, Wang J, Liu Y, Dong Y. Geometric correction in normalization for long axial field-of-view, whole-body PET scanner. In: *2019 IEEE Nuclear Science Symposium and Medical Imaging Conference (NSS/MIC)*. Sydney, AU:IEEE;2019.
31. He L, Deng Z, Ding Y, Zhao Y, Hu D, Dong Y. Validation of scatter correction with Monte Carlo simulation for uEXPLORER. *J Nucl Med*. 2019;60(suppl 1):45.
32. Zhang X, Zhou J, Cherry SR, Badawi RD, Qi J. Quantitative image reconstruction for total-body PET imaging using the 2-meter long EXPLORER scanner. *Phys Med Biol*. 2017;62:2465-2485.
33. Zhao Y, Deng Z, Lv Y, Hu D, Ding Y, Dong Y. Image Quality evaluation of analytic reconstruction algorithms for long axial field-of-view PET scanner. *J Nucl Med*. 2019;60(suppl 1):240.
34. Defrise M, Kinahan PE, Townsend DW, et al. Exact and Approximate rebinning algorithms for 3-D PET data. *IEEE Trans Med Imaging.* 1997;16:145-158.
35. Berg E, Zhang X, Bec J, et al. Development and evaluation of mini-EXPLORER: a long axial field-of-view PET scanner for nonhuman primate imaging. *J Nucl Med*. 2018;59:993–998.

FIGURE 1. Photograph of the uEXPLORER total-body PET/CT scanner installed at the EXPLORER Molecular Imaging Center in Sacramento, CA, USA.

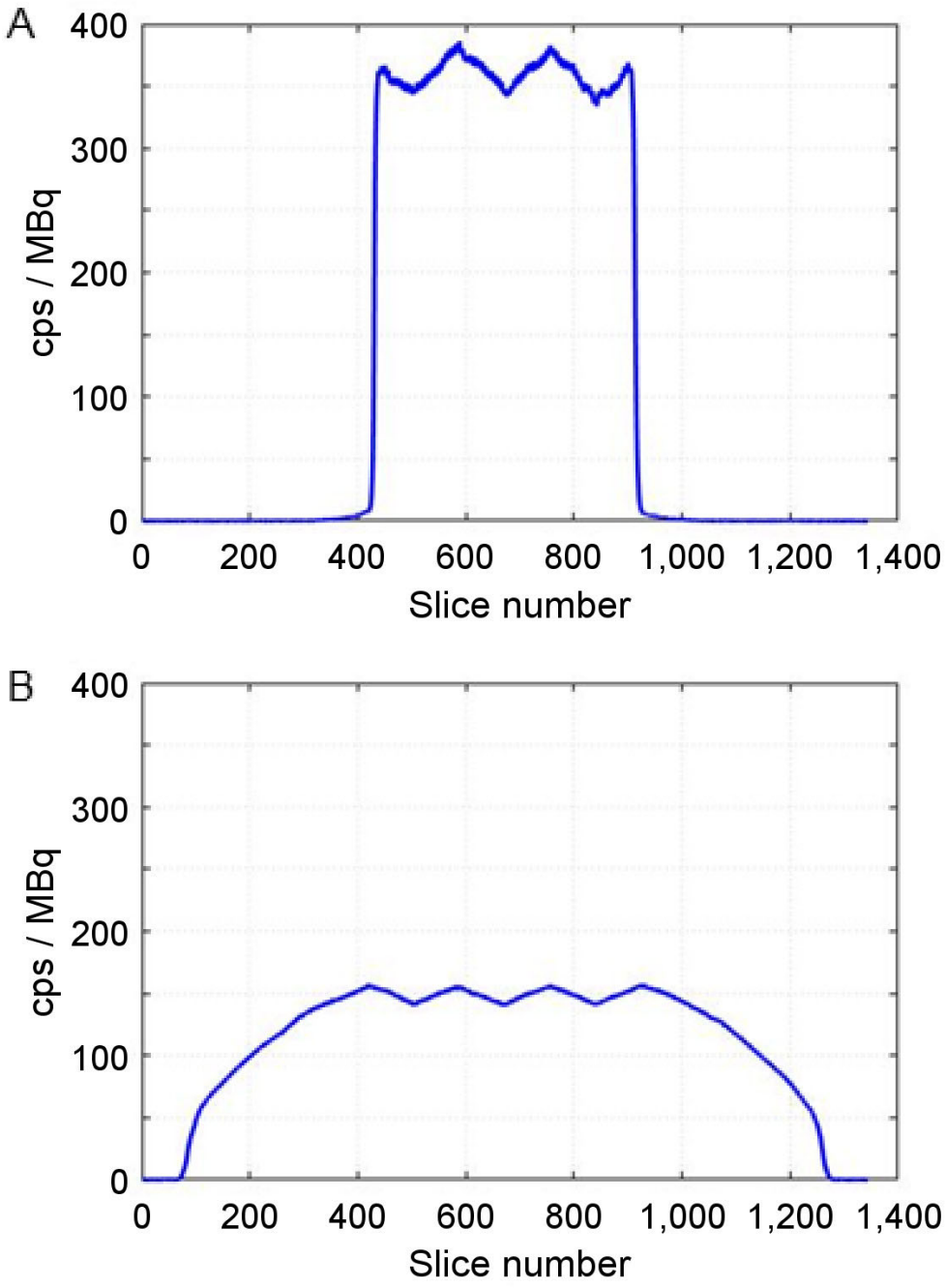

FIGURE 2. Axial sensitivity profiles for the (A) 70 cm (NEMA NU-2-2018) and (B) 170 cm line source phantoms. The sinogram slice thickness is 1.444 mm.

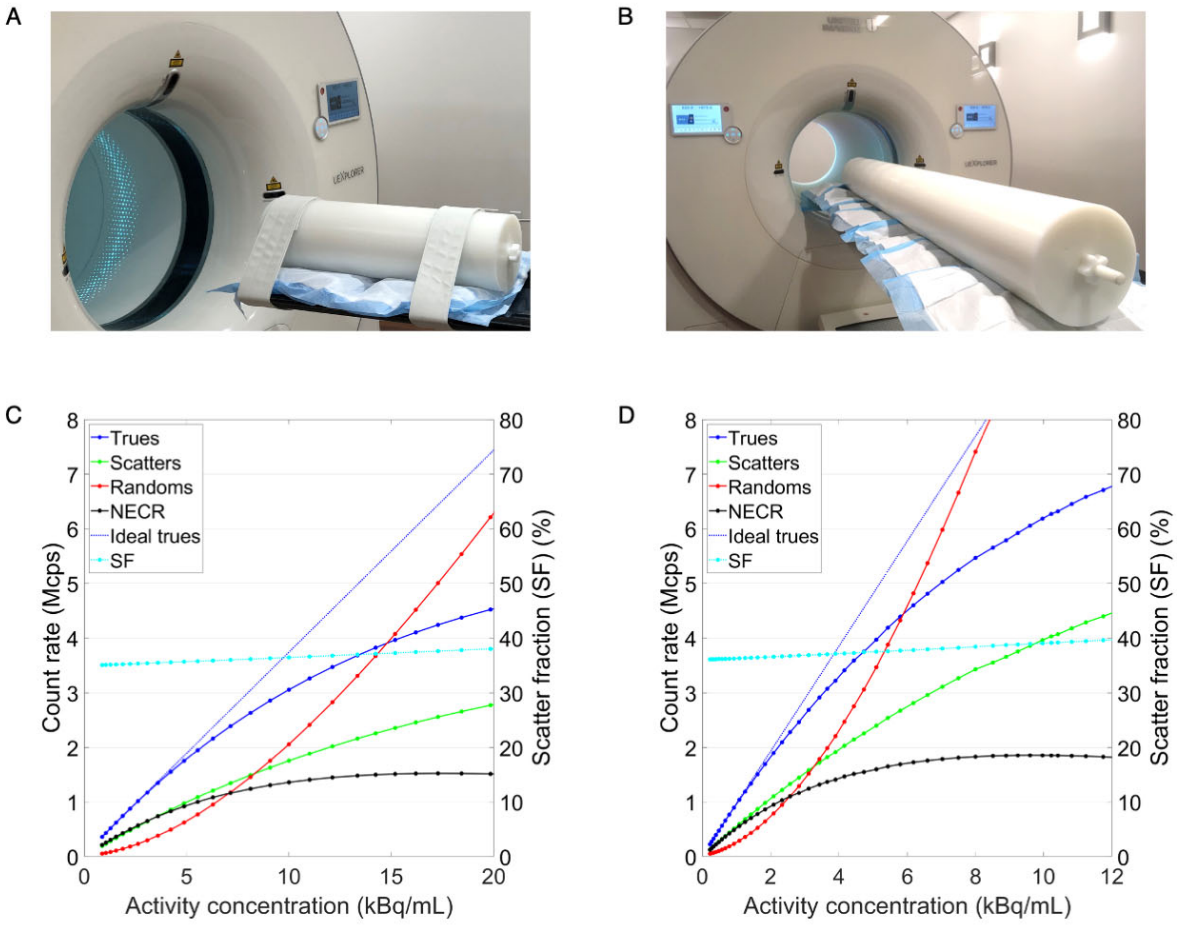

FIGURE 3. (A) The 70 cm-long NEMA NU-2 scatter phantom and (B) the 175 cm-long scatter phantom assembled from multiple NEMA NU-2 phantoms on the uEXPLORER PET/CT patient bed. Measured count-rates with (C) the 70 cm-long scatter phantom and (D) the 175 cm-long scatter phantom. Count-rate measures are plotted vs. the left vertical axes, scatter fraction (SF) are plotted vs. the right vertical axes. Activity concentrations for (A) and (B) were computed by dividing the total activity in the phantom at each time-point by the phantom volume (22L for the 70 cm long phantom, and 55L for the 175 cm long phantom).

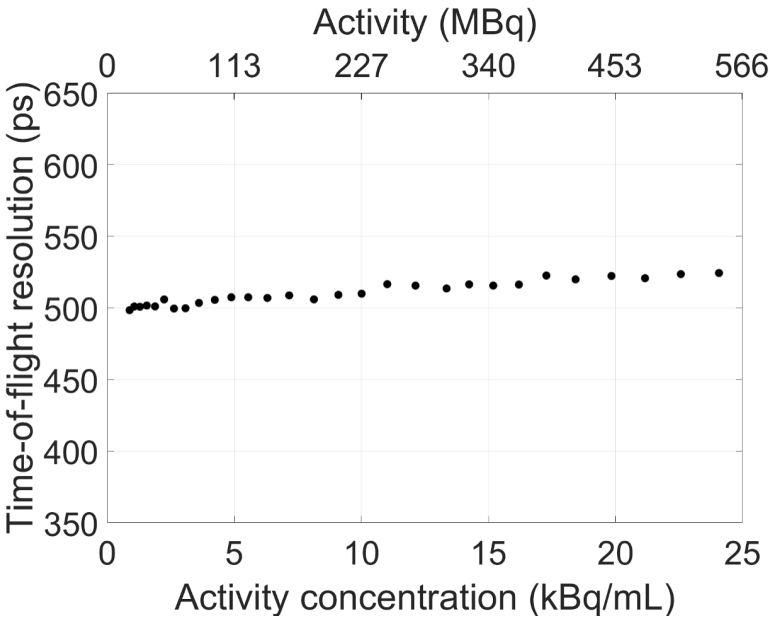

FIGURE 4. Time-of-flight resolution plotted vs activity concentration using the 70 cm-long NEMA NU-2 scatter phantom. A TOF resolution of 505 ps at 5.3 kBq/mL was obtained.

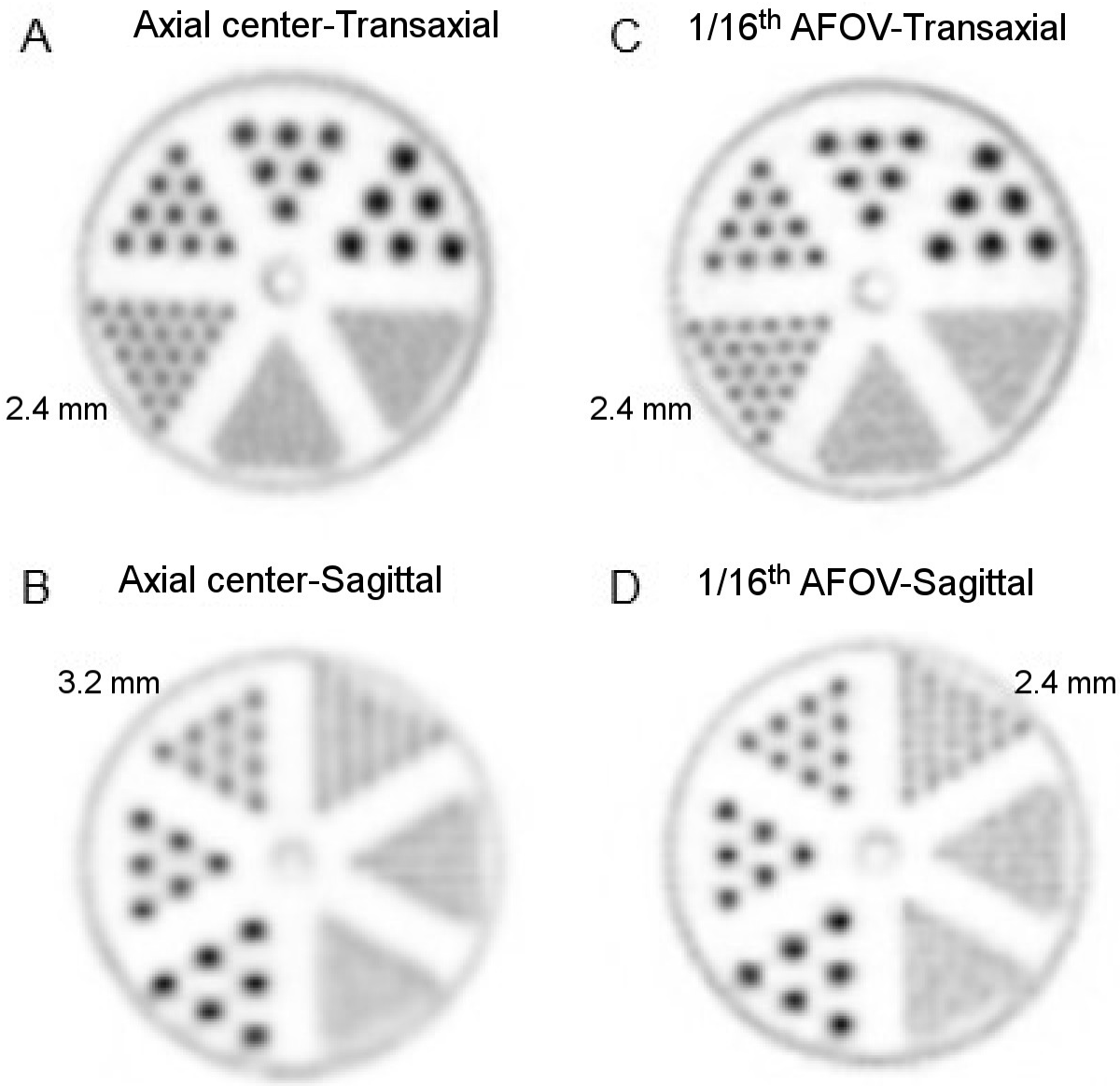

FIGURE 5. Reconstructed image slices of the Mini-Derenzo phantom imaged at the axial center (left column A,B), and 1/16th of the AFOV (right column C,D), and with two orientations transaxial (top row, A,C) and sagittal (bottom row B,D). Image slice thickness is 1.172 mm.

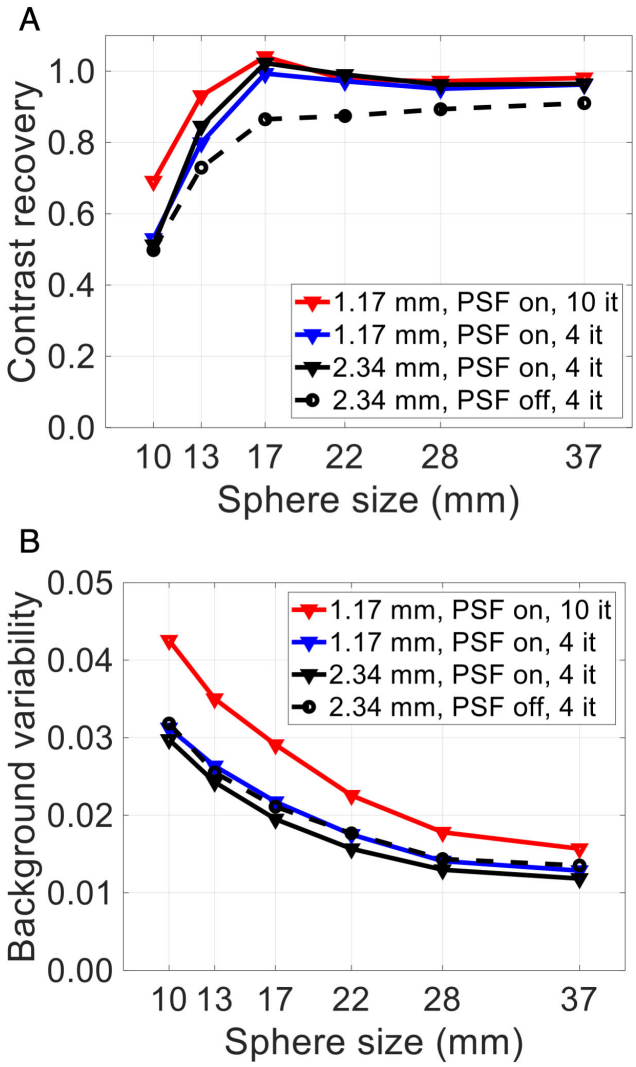

FIGURE 6. (A) Contrast recovery and (B) background variability measured with the standard NEMA IQ phantom evaluation – phantom placed at the center of the AFOV scanned for 30-min.

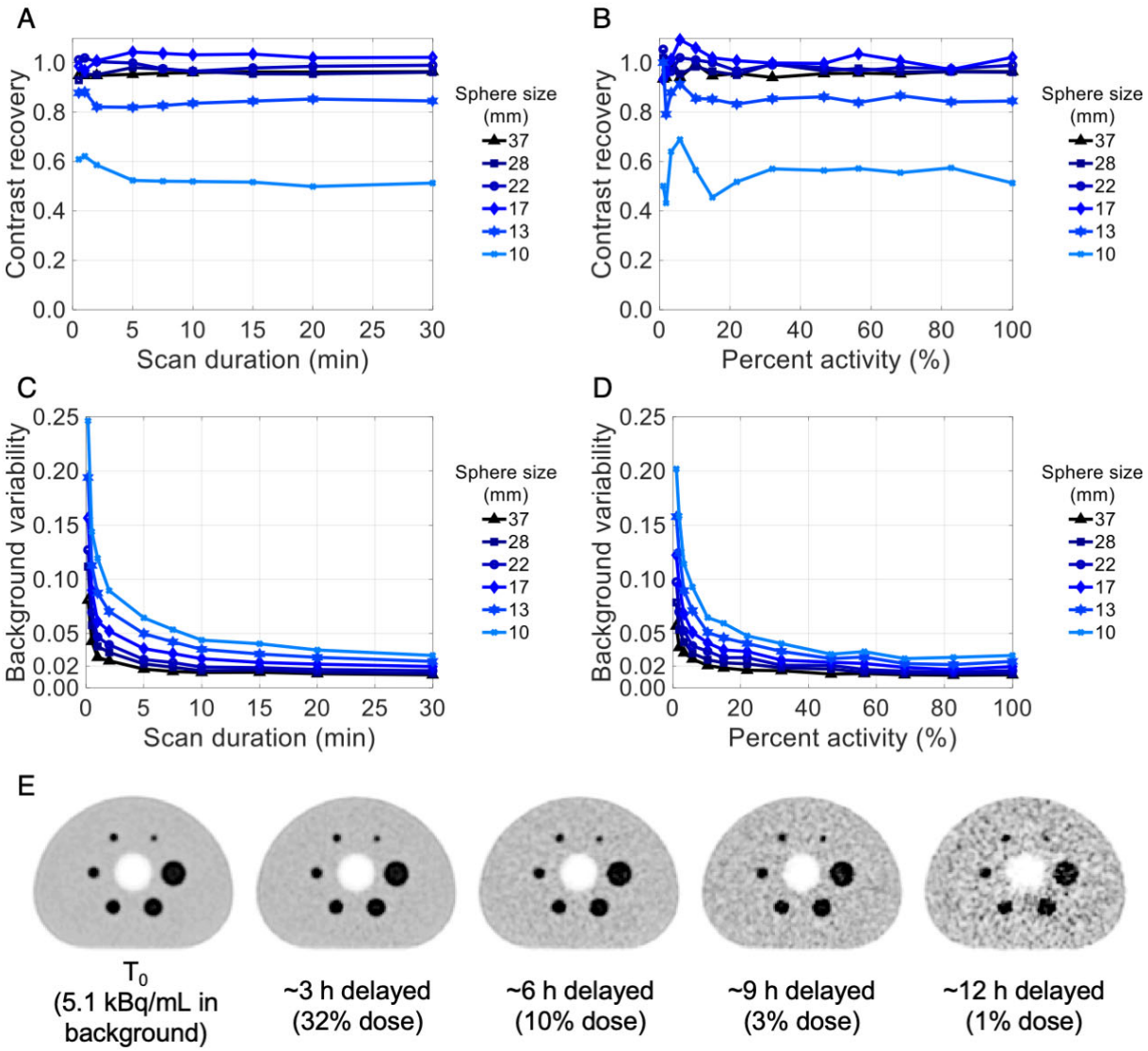

FIGURE 7. (A,B) Contrast recovery and (C,D) background variability as a function of (A,C) scan duration and (B,D) activity. The percent activity is relative to the initial activity in the phantom at the starting time of the scans. (E) Transaxial image slices of the 30-min scan at several imaging timepoints reconstructed using the clinical reconstruction protocol. All images are decay corrected and use the same color scale: 0 – 20 kBq/mL.

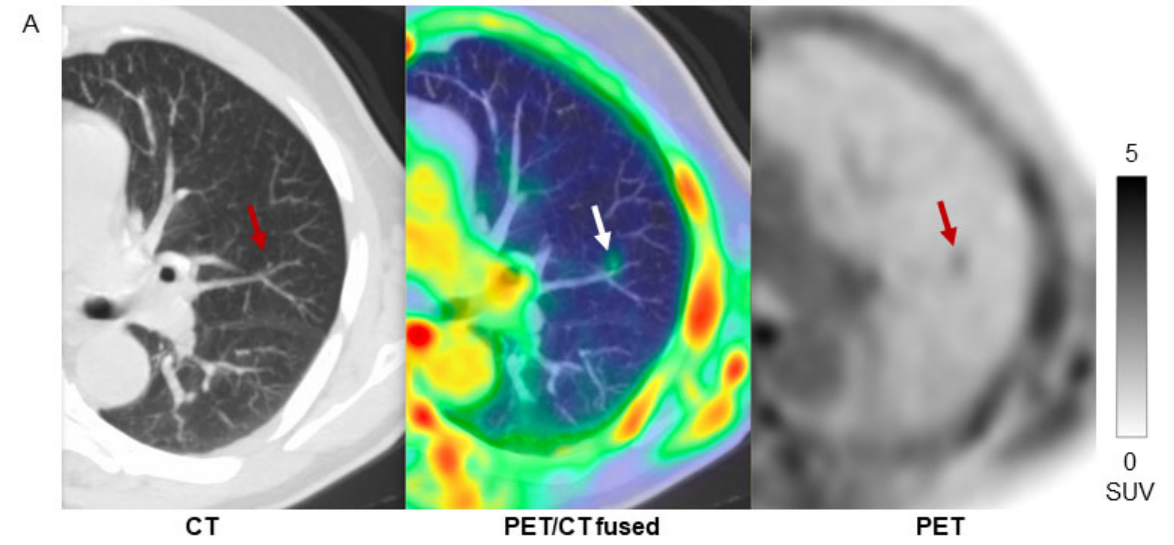
A
5
0
SUV
CT
PET/CT fused
PET

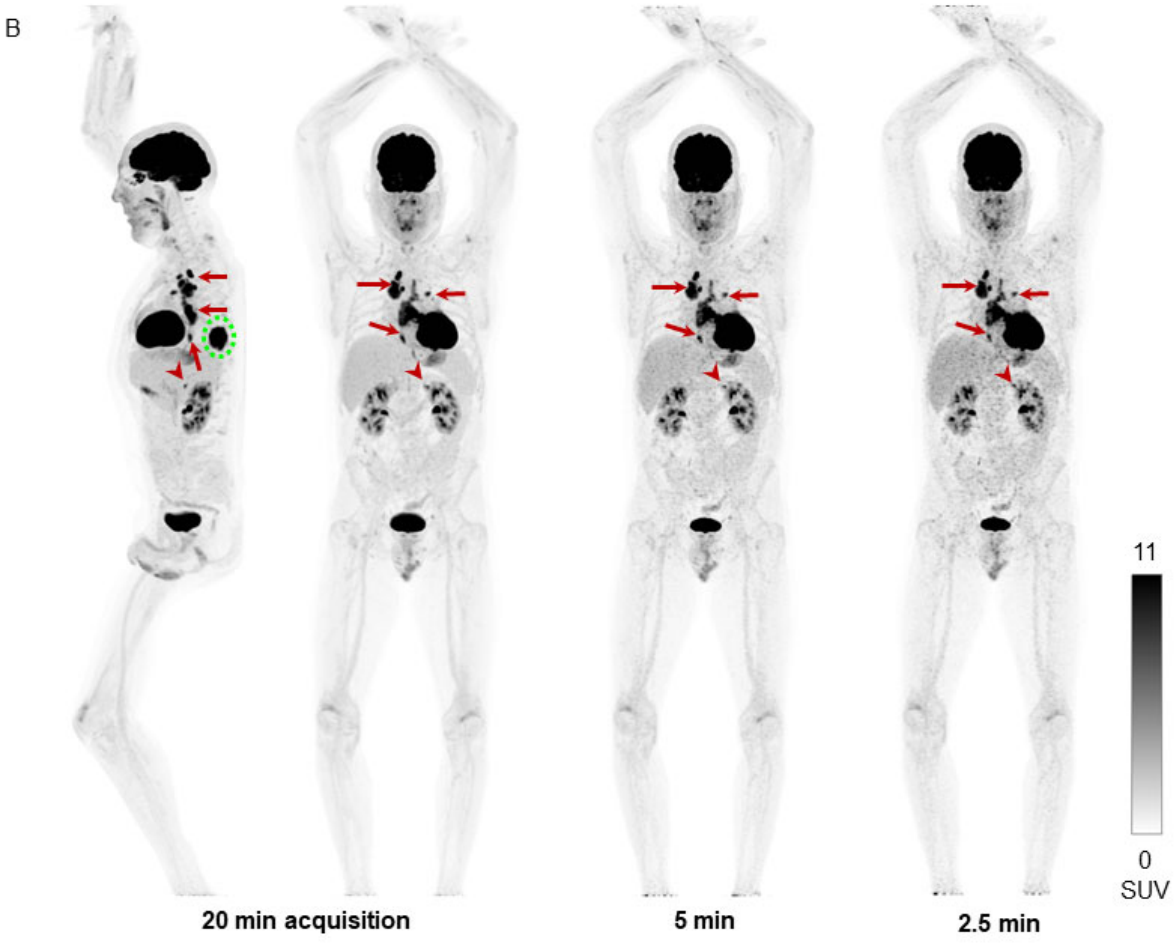
B
11
0
SUV
20 min acquisition
5 min
2.5 min

FIGURE 8. Human imaging examples exemplifying the performance of the uEXPLORER total-body PET scanner. An axial slice from ^{18}F-fluciclovine PET (right) with the corresponding fused (middle) and CT images (left) of a 68-year-old male patient with castration-resistant metastatic prostate cancer (A) demonstrating clear visualization of ^{18}F-Flucicovine accumulation within a 2.5 mm diameter pulmonary nodule. A maximum-intensity-projection (MIP) of a representative clinical oncology ^{18}F-FDG PET scan (B) reconstructed with 20-, 5-, and 2.5-min scan durations. Images show the primary left lower lobe lung tumor (dashed green circle), with multiple variable-sized (0.8-6 cm) hilar, mediastinal and lower esophageal nodal metastases (arrows), and a ~1 cm FDG-avid left adrenal nodule (arrowhead) which is visualized for all scan durations.

TABLE 1. Spatial resolution of ^{18}F point sources measured with FORE-FBP reconstruction.

Location	Position	FWHM (mm)		
		Tangential	Radial	Axial
Center AFOV	1 cm	3.0	3.0	2.8
	10 cm	3.1	3.4	3.2
	20 cm	4.0	4.7	3.2
1/8th AFOV	1 cm	2.9	3.0	2.9
	10 cm	3.2	3.6	3.1
	20 cm	4.4	4.6	3.3

TABLE 2. Contrast recovery and background variability at five locations along the AFOV.

Axial Position	Background activity concentration (kBq/mL)	Scan duration	37 mm Sphere		22 mm Sphere	
			CRC	Background Variability	CRC	Background Variability
-63 cm (2/10^{ths} AFOV)	3.3	10.5-min	96.8%	1.4%	94.7%	2.8%
-39 cm (3/10^{ths} AFOV)	3.6	9.6-min	96.7%	1.7%	96.8%	2.4%
0 cm (center)	4.5	7.6-min	95.8%	1.6%	98.9%	1.9%
+39 cm (7/10^{ths} AFOV)	2.9	11.7-min	94.7%	1.6%	96.7%	2.4%
+63 cm (8/10^{ths} AFOV)	2.7	13.0-min	91.5%	1.8%	90.4%	2.5%

TABLE 3. Table of imaging parameters associated with the images displayed in Figure 8. Count rates were extracted from the listmode tags, deadtime fractions were estimated according to the deadtime fractions at the equivalent activity concentration with the 175 cm scatter phantom.

Figure	Image	Injected Dose	Subject Weight	Timepoint	Scan Duration	Singles/Prompts/Randoms	Deadtime Fraction
8(A)	Trans axial slices	320 MBq ^{18}F-fluciclovine	76 kg	4-min post-inj.	10-min	101/24.7/18.3 Mcps	14.4%
8(B)	MIP	188 MBq ^{18}F-FDG	93 kg	90-min post-inj.	20-, 5-, & 2.5-min	19.6/4.4/2.2 Mcps	1.2%

Supplementary Material

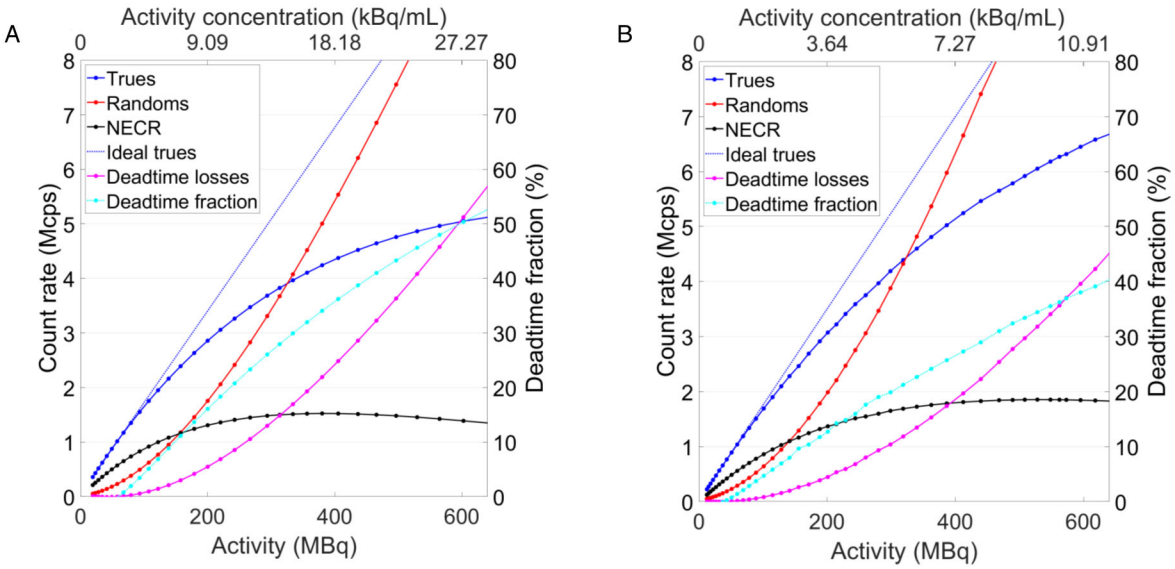

Supplemental Figure 1 - Measured count-rates and deadtime losses as a function of total ^{18}F activity with the (A) 70 cm-long scatter phantom with a volume of 22 L and (B) the 175 cm-long scatter phantom with a volume of 55 L. The ideal trues count-rate is estimated from a linear fit to the trues rate at low activities when deadtime affects are negligible, deadtime losses are then the difference between the ideal and measured trues in Mcps, and the deadtime fraction is the fractional deadtime loss relative to the ideal trues count rate.

Supplemental TABLE 1. Specifications of the NEMA image quality scans performed at the center of AFOV to assess the effect of sphere-to-background ratio on contrast recovery.

Sphere-to-background ratio	Background activity concentration (kBq/mL)	Scan duration (min)
3.7:1	5.1	30
5.2:1	4.5	30
9.0:1	4.5	30

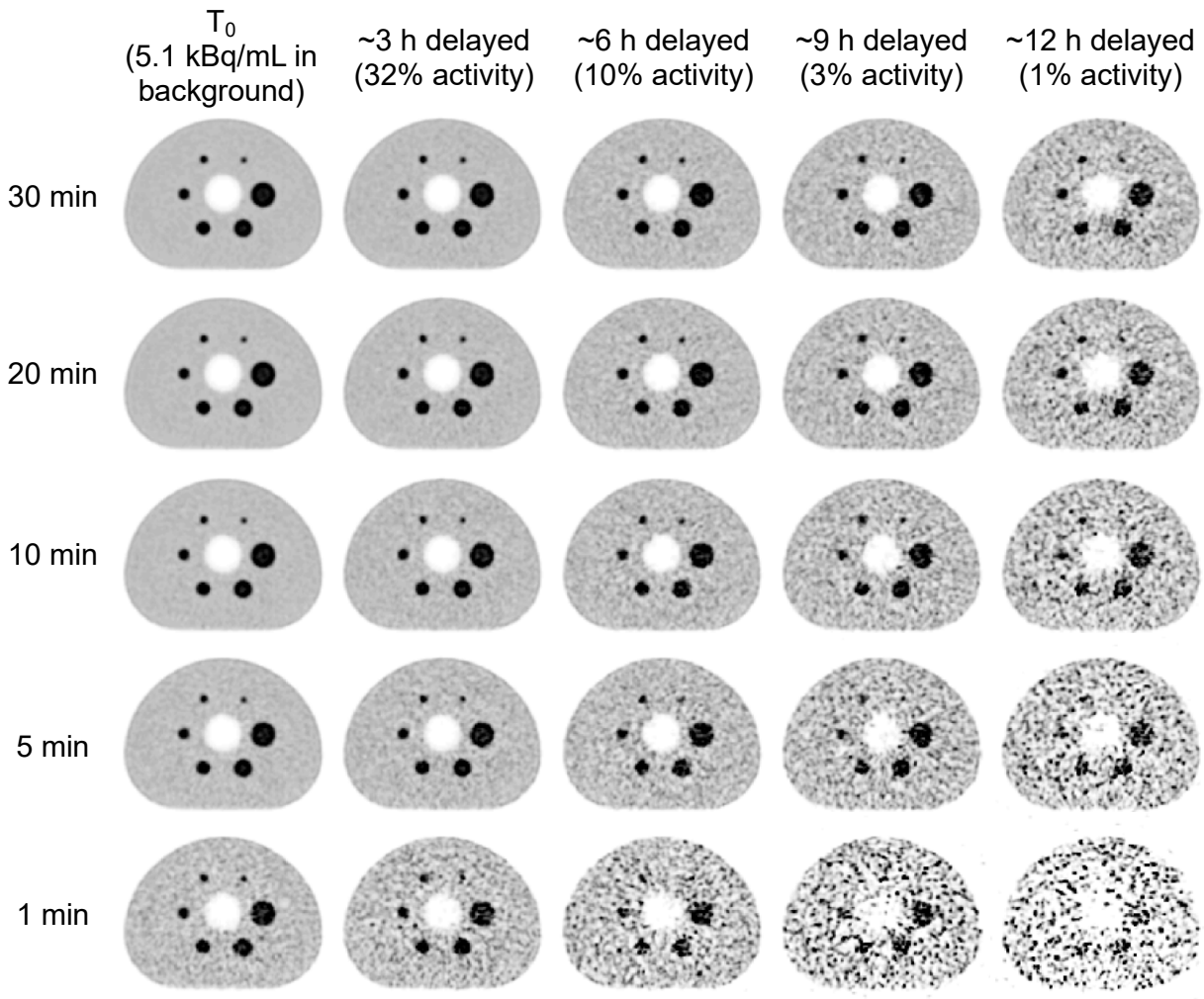

Supplemental Figure 2 – Transaxial image slices of a 30-min scan of the NEMA IQ phantom at the center of AFOV at several imaging timepoints, compared to reduced scan durations of 20, 10, 5, and 1 min. All images were reconstructed using the clinical image reconstruction protocol (2.34-mm isotropic voxels, 4 iterations) with PSF modelling and they were decay corrected to be shown using the same color scale: 0 – 20 kBq/mL. The phantom was filled with a sphere-to-background ratio of 3.7:1 and had background activity concentration of 5.1 kBq/mL at the start of the scans.

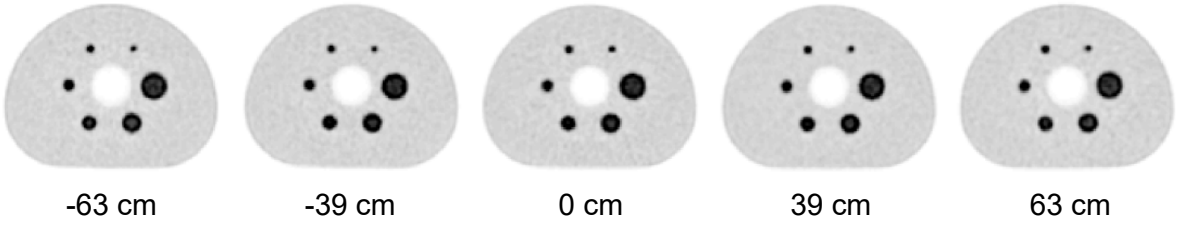

Supplemental Figure 3 – Transaxial image slices of the NEMA IQ phantom scanned at five axial positions throughout the AFOV. The offset from the center of AFOV is shown below each image indicating the scan position. All images were reconstructed using the clinical image reconstruction protocol (2.34-mm isotropic voxels, 4 iterations) with PSF modelling and they were decay corrected to be shown using the same color scale: 0 – 27 kBq/mL. The phantom was filled with a sphere-to-background ratio of 5.2:1 and had background activity concentration of 4.5 kBq/mL at the start of the scans.

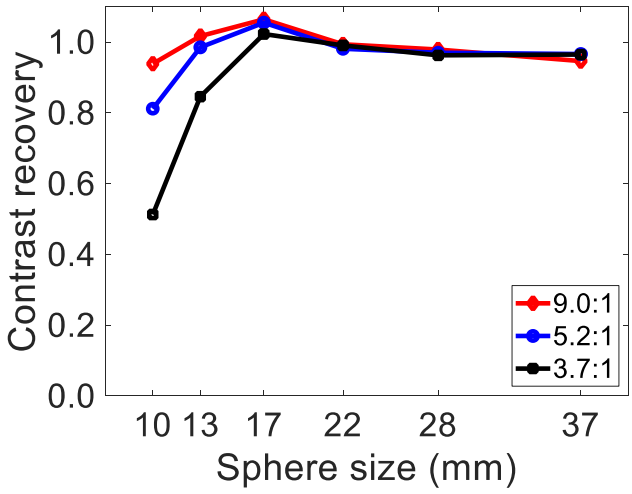

Supplemental Figure 4 – Contrast recovery measured in the NEMA IQ phantom for different sphere-to-background ratios. The contrast recovery measurements in the phantom filled with 9.0:1 sphere-to-background ratio were slightly affected by presence of an air bubble in the largest sphere. All images were reconstructed using the clinical image reconstruction protocol (2.34-mm isotropic voxels, 4 iterations) with PSF modelling.

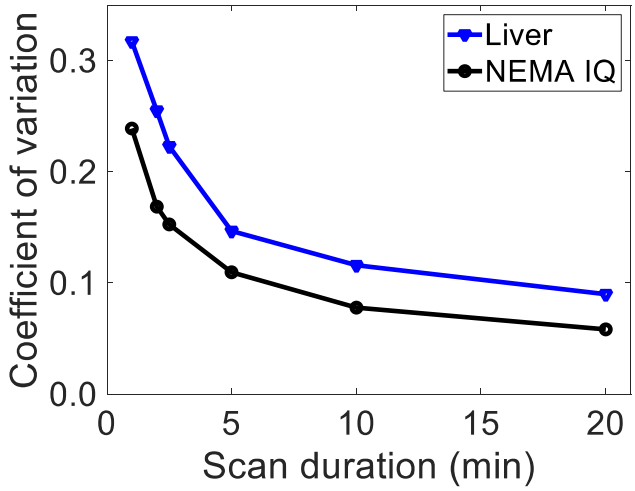

Supplemental Figure 5 – Coefficient of variation (CV) of a 37-mm diameter spherical ROI placed in the patient liver and in the NEMA IQ phantom background and reconstructed with shortened scan durations. The average activity concentration measured from the image of the patient liver was 3.64 kBq/mL, compared to 3.56 kBq/mL for the NEMA IQ background.